Chemical Science

ROYAL SOCIETY OF CHEMISTRY

EDGE ARTICLE

View Article Online
View Journal

Cite this: DOI: 10.1039/d6sc01125j

All publication charges for this article have been paid for by the Royal Society of Chemistry

Constructing interfacial charge transfer channels *via* plasmon-mediated dual excitation in S-vacancy-rich $ZnIn_2S_4$/CuSe heterostructures for enhanced NIR-driven H_2 production

Yuanyong Huang,†[a] Cai Ning,†[a] Xinyu Lu,[a] Yang Chao,[a] Junhao He,[a] Qiankun Gao,[a] Yu Yu,[a] Zhongkai Xie,[a] Hailing Huo[a] and Weidong Shi *[ab]

Conventional photocatalysts are inherently inefficient at harnessing the predominant near-infrared (NIR) component of sunlight, and their intrinsic kinetic and thermodynamic barriers further impose a severe constraint on solar-to-hydrogen (H_2) conversion efficiency. However, the rational design of highly efficient, durable NIR-responsive photocatalysts that avoid scarce metal cocatalysts and toxic dyes remains a pivotal challenge. Herein, we demonstrate a new strategy for constructing a strong interfacial coupled heterojunction that strategically integrates plasmonic CuSe with S-vacancy-rich $ZnIn_2S_4$ (Vs-$ZnIn_2S_4$) to enhance NIR-driven H_2 evolution through a plasmon-mediated dual excitation (PMDE) mechanism. As evidenced by ultrafast femtosecond transient absorption (fs-TA) spectroscopy and density functional theory (DFT) calculations, the rational heterointerface engineering gives rise to fast charge-transfer channels, which in turn lower the reaction energy barrier, suppress carrier recombination, and induce interfacial charge redistribution. These improvements collectively contribute to an optimized heterojunction that achieves an apparent quantum efficiency of 3.0% at 940 nm, surpassing all state-of-the-art noble-metal-free photocatalysts operating beyond 900 nm reported to date. The composite maintains its structural and catalytic integrity even under strong acidic/alkaline conditions (*e.g.*, pH = 1 and pH = 12) and in high-salinity environments (*e.g.*, 5.0 M NaCl solution), setting a benchmark for ultrastable NIR light-harvesting photocatalysts. This work provides novel insights into optimizing charge separation, stabilization, and accumulation during NIR-driven H_2 production *via* PMDE.

Received 8th February 2026
Accepted 6th March 2026

DOI: 10.1039/d6sc01125j

rsc.li/chemical-science

Introduction

The global shift toward low-carbon development is driven by pressing challenges from climate change, the energy crisis, and greenhouse gas emissions.[1–3] Solar-driven water splitting offers an environmentally friendly, sustainable, and scalable route to produce hydrogen (H_2), positioning it as a critical component of future energy systems.[4] Although photocatalytic efficiency is fundamentally determined by light harvesting, extending spectral absorption into the near-infrared (NIR) region (800–2500 nm) has become a central research target, as NIR photons account for 52% of total solar irradiance—far surpassing the UV/visible components.[5–10] However, NIR-driven photocatalysis suffers from mismatched energetics and suboptimal efficiency, often due to the difficulty in balancing photon absorption, charge excitation, and surface reactions.[11] Despite over four decades of research, NIR-active photocatalysts for solar H_2 generation have achieved only limited progress, with both activity and stability still falling below expectations.[12–23] Therefore, developing an efficient, scalable, and stable photocatalytic system capable of effectively utilizing NIR light remains a critical goal in renewable energy research. The key challenge lies in designing photocatalytic systems that can efficiently capture and utilize low-energy NIR photons to drive water splitting reactions at an industrial scale, while maintaining both high activity and long-term stability.

To date, NIR-driven photocatalytic water splitting for H_2 production has primarily relied on plasmonic noble metals (*e.g.*, Pt, Au, Ag) or organic dye sensitizers (*e.g.*, porphyrins, phthalocyanines).[24–27] Unfortunately, these systems suffer from high costs, toxicity, and photocorrosion, severely hindering catalyst sustainability and large-scale practical applications. To address these challenges, developing robust, noble metal-free NIR-active photocatalysts *via* tailored nanostructures and

[a]College of Environmental and Chemical Engineering, Jiangsu University of Science and Technology, Zhenjiang, 212003, P.R. China. E-mail: swd1978@ujs.edu.cn

[b]School of Chemistry and Chemical Engineering, Jiangsu University, Zhenjiang, 212013, P.R. China

† Y. Huang and C. Ning contributed equally to this work.

interfacial engineering has become a key research direction. For instance, Zhu *et al.* pioneered a 2D/2D black phosphorus/carbon nitride (BP/CN) van der Waals heterostructure, achieving efficient NIR-driven H_2 evolution (0.15 μmol h^{-1}) at λ > 780 nm for over 3 h.[28] Liu *et al.* recently developed ultrathin $CuCrP_2S_6$ nanosheets with efficient charge transfer and long carrier lifetime, attaining a 1.03% apparent quantum efficiency (AQE) under λ = 800 nm with 16 h stability.[29] Unfortunately, state-of-the-art non-precious metal NIR photocatalysts face three critical limitations: insufficient light-harvesting (λ < 800 nm), AQE values lower than 1% under NIR light, and inferior stability. These shortcomings arise from the unoptimized interplay between photon utilization, charge transport, and structural stability. To move beyond these constraints, a paradigm shift from optimizing single-component NIR-absorbing photocatalysts toward holistic multiscale engineering is imperative. Synergistic strategies involving energy band engineering, defect-state design, and heterostructural modification collectively drive simultaneous advancements in NIR photon-to-energy conversion efficiency and operational durability. However, no ultrastable noble metal-free system has yet achieved an NIR-driven AQE exceeding 2% through multiscale engineering strategies, despite their importance and high desirability.

As of the latest available research, copper chalcogenide nanocrystals (*e.g.*, CuS, $Cu_{1.8}S$, $Cu_{7.2}S_4$, Cu_9S_5, CuSe) have emerged as earth-abundant alternatives to noble metals, with strong LSPR characteristics and good structural stability.[14,15,18,23,30] Endowed with intrinsic functional properties including high charge carrier mobility and potentially high carrier concentrations, these materials also exhibit superior electrical conductivity, rendering them ideal candidates for NIR-driven photocatalysis. For example, Lian *et al.* fabricated a CuS@ZnS core–shell nanocrystal composite modified with Pt cocatalysts, which delivered robust photocatalytic performance (0.13 μmol h^{-1}).[14] Despite these encouraging results, single-component NIR-excited copper chalcogenides still suffer from severely low photocatalytic activity (<1%), which stems from non-radiative energy transfer and falls well short of practical application requirements.[10] Plasmon-mediated dual-excitation (PMDE) systems, which integrate the plasmonic effects of copper chalcogenides with compatible NIR-responsive semiconductor acceptors, are hypothesized to be a viable strategy for generating more surviving charge carriers. However, to the best of our knowledge, no reports have documented plasmonic copper chalcogenide composites that harness dual-excitation pathways to achieve highly efficient and ultrastable NIR-driven H_2 evolution at wavelengths above 800 nm.

As a proof-of-concept study, the Vs-$ZnIn_2S_4$@CuSe nanocomposite was rationally designed and fabricated using a simple hydrothermal process (Fig. 1a) and employed for NIR-driven H_2 production. A suite of characterization techniques was used to probe the morphology, structure, composition, and optical properties of the Vs-$ZnIn_2S_4$@CuSe heterojunctions. The robust interfacial coupling interactions within the Vs-$ZnIn_2S_4$@CuSe catalysts give rise to rapid, irreversible charge transfer pathways, effectively suppressing charge carrier recombination;

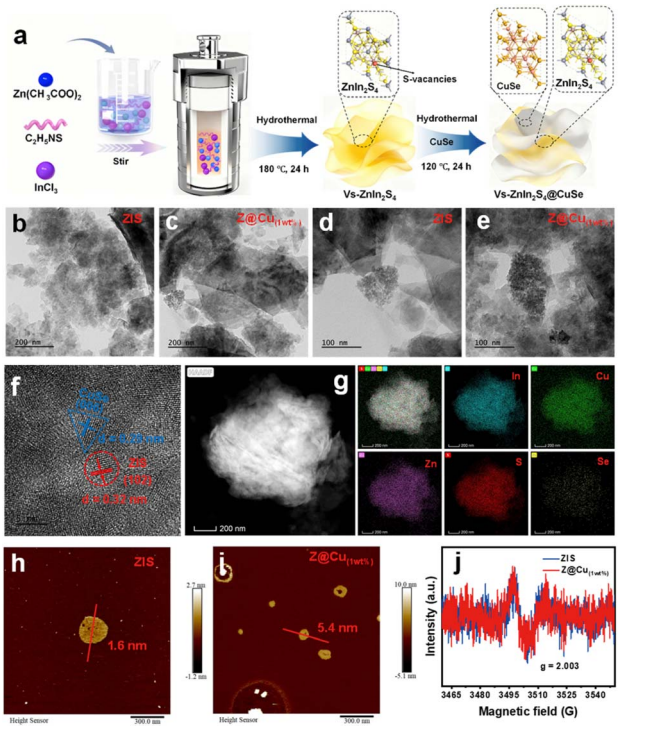

Fig. 1 (a) Diagram of the formation of NIR-responsive Vs-$ZnIn_2S_4$@CuSe heterostructured photocatalysts. The morphological, structural, and elemental characteristics of the as-prepared samples are shown. Typical TEM images of pure Vs-$ZnIn_2S_4$ (b and c) and its composite with 1 wt% CuSe (d and e). Representative HRTEM images of Vs-$ZnIn_2S_4$@CuSe (f), showing the lattice fringes of $ZnIn_2S_4$ and CuSe phases. (g) HAADF-STEM and EDX elemental mapping images of Zn, In, S, Cu, and Se in Vs-$ZnIn_2S_4$@CuSe. Scale bar: 200 nm. AFM images of ZIS (h) and Z@$Cu_{(1\ wt\%)}$ (i). (j) EPR measurements of Vs-$ZnIn_2S_4$ and Z@$Cu_{(1\ wt\%)}$.

meanwhile, the interfacial carrier dynamics were systematically probed *via* ultrafast femtosecond transient absorption (fs-TA) spectroscopy and density functional theory (DFT) calculations. The optimized heterojunction achieves the highest reported apparent quantum efficiency (AQE) of 3.0% at λ = 940 nm, setting a new benchmark for noble metal-free hybrid photocatalysts operating at wavelengths beyond 900 nm. This work presents a novel strategy for designing efficient heterojunctions for NIR-driven H_2 production *via* a PMDE mechanism.

Results and discussion

Construction and structural characterization of Vs-$ZnIn_2S_4$@CuSe heterostructures

As shown in Fig. S1, CuSe, synthesized *via* a hydrothermal method, exhibits a hexagonal phase (Joint Committee on Power Diffraction Standards (JCPDS) No. 34-0171), which is characteristic of CuSe.[31,32] The Vs-$ZnIn_2S_4$@CuSe composite predominantly exhibits the hexagonal phase of $ZnIn_2S_4$ (JCPDS No. 72–0773).[7,33] The diffraction peaks for Z@$Cu_{(1\ wt\%)}$ are observed to be weaker in the composite compared to pure Vs-$ZnIn_2S_4$, suggesting that the presence of CuSe slightly alters the crystal structure of $ZnIn_2S_4$. This reduction in peak intensity may

indicate changes in crystallinity or a decrease in crystallite size due to CuSe incorporation. Inductively coupled plasma optical emission spectroscopy (ICP-OES) yielded a Cu : Se ratio of 1.02 : 1, indicating a virtually stoichiometric 1 : 1 composition. Scanning electron microscopy (SEM) images show that both pure $ZnIn_2S_4$ and CuSe, and the Vs-$ZnIn_2S_4$@CuSe composites exhibit a sheet-like structure (Fig. S2). As the CuSe content increases, the stacking degree of the layers in the composite material also increases, suggesting the self-assembly nature of the material.

Transmission electron microscopy (TEM) and high-resolution TEM (HRTEM) images (Fig. 1b–f) reveal that the Vs-$ZnIn_2S_4$@CuSe composite has a thicker layered structure compared to the pure Vs-$ZnIn_2S_4$ (Fig. S3). The images confirm the successful integration of CuSe into the Vs-$ZnIn_2S_4$ structure. The lattice spacings observed in the HRTEM images are 0.32 nm, corresponding to the (102) crystal planes of $ZnIn_2S_4$, and 0.29 nm, corresponding to the (006) crystal planes of CuSe, respectively. These lattice spacings further support the successful formation of the Vs-$ZnIn_2S_4$@CuSe nanohybrid. Energy dispersive X-ray (EDX) elemental mapping confirms the uniform distribution of Zn, In, S, Cu, and Se across the composite surface. This uniform distribution indicates that CuSe is effectively integrated with Vs-$ZnIn_2S_4$ (Fig. 1g and S4). The thickness of Vs-$ZnIn_2S_4$ and Z@$Cu_{(1\ wt\%)}$ was evaluated by atomic force microscopy (AFM). AFM images reveal that pure Vs-$ZnIn_2S_4$ has a thickness of approximately 1.6 nm, and the nanocomposite Z@$Cu_{(1\ wt\%)}$ shows an increased thickness of about 5.4 nm, suggesting that CuSe incorporation results in a thicker, more layered material (Fig. 1h and i). Additionally, electron paramagnetic resonance (EPR) measurements were used to confirm the presence of sulfur (S) vacancies in the Vs-$ZnIn_2S_4$@CuSe composites. A slightly stronger signal at $g = 2.003$ was observed for the Vs-$ZnIn_2S_4$@CuSe composite compared to pure Vs-$ZnIn_2S_4$, suggesting a higher concentration of paramagnetic centers (Fig. 1j).[14]

X-ray photoelectron spectroscopy (XPS) provides detailed information on the valence states and surface chemical compositions of the Vs-$ZnIn_2S_4$@CuSe composites. As shown in Fig. S5a, the Cu 2p spectrum of CuSe nanosheets exhibits two characteristic peaks: Cu $2p_{3/2}$ at 931.9 eV and Cu $2p_{1/2}$ at 952.4 eV, corresponding to the Cu^{2+} species. These peaks confirm that CuSe predominantly exists in the Cu^{2+} oxidation state.[34] The Cu 2p peaks of the Vs-$ZnIn_2S_4$@CuSe composites shift to lower binding energies by approximately 0.1 eV compared to pure CuSe, suggesting the formation of an interface between CuSe and Vs-$ZnIn_2S_4$ due to their electronic interactions. As shown in Fig. S5b, the Zn $2p_{3/2}$ and Zn $2p_{1/2}$ peaks of pure Vs-$ZnIn_2S_4$ are observed at 1021.3 eV and 1044.4 eV, respectively, indicating the presence of Zn^{2+} ions.[35] In the Vs-$ZnIn_2S_4$@CuSe composites, these Zn 2p peaks shift to higher binding energies by about 0.1 eV. This shift suggests that the Zn^{2+} ions are influenced by the interaction with CuSe, resulting in a modified electronic environment around Vs-$ZnIn_2S_4$. This shift also implies the formation of a built-in electric field between CuSe and Vs-$ZnIn_2S_4$, which facilitates the transfer of photogenerated carriers at the interface, a similar phenomenon to that previously reported in plasmonic composite materials (such as WO_3@$ZnIn_2S_4$).[36] The In 3d spectrum of Vs-$ZnIn_2S_4$ is deconvoluted into two peaks at 452.2 eV and 444.7 eV, which correspond to the In^{3+} oxidation state (Fig. S5c).[37] In the composites, the In 3d peaks shift to higher binding energies, similar to the behavior observed for the Zn 2p peaks. This shift further supports the formation of the built-in electric field, influencing the electronic states of In^{3+} in the Vs-$ZnIn_2S_4$ counterpart. The S 2p spectrum of the composites shows an S $2p_{3/2}$ peak at 161.5 eV and S $2p_{1/2}$ peak at 162.8 eV (Fig. S5d). These binding energies are slightly higher than those observed in pure Vs-$ZnIn_2S_4$, indicating a shift in the chemical environment of S^{2-} due to the interaction with CuSe.[38] The Cu 2p, Zn 2p, In 3d, and S 2p peaks all exhibit shifts in binding energy upon the formation of the Vs-$ZnIn_2S_4$@CuSe composite, indicating electronic interactions between CuSe and Vs-$ZnIn_2S_4$.

Optical characteristics and photoactivity evaluation

The ability of a photocatalyst to capture NIR photons is one of the most crucial factors in NIR-driven water splitting to produce H_2.[39] As shown in Fig. 2a, CuSe exhibits strong absorption in the NIR region, making it an effective material for NIR photon harvesting. In contrast, Vs-$ZnIn_2S_4$ demonstrates weak NIR absorption on its own. However, when combined in the Vs-$ZnIn_2S_4$@CuSe composites, the overall NIR light harvesting capacity is markedly enhanced, particularly with increasing CuSe loading from 0.5 wt% to 2 wt%. This enhancement is due to the LSPR effect of CuSe, which allows it to absorb more NIR light.[40] When these plasmonic materials are excited by NIR photons, their free electrons resonate with the incident light, leading to enhanced light absorption and increased electron generation for the photocatalytic process.[41] As a result, the Vs-$ZnIn_2S_4$@CuSe composites can achieve enhanced broad-spectrum light harvesting, including NIR light, which is typically underutilized in conventional photocatalysts.

Photocatalytic performance was evaluated under NIR irradiation (λ > 800 nm) using triethanolamine (TEOA) as a sacrificial agent. As shown in Fig. 2b, pure-phase CuSe produced 0.58 μmol of H_2 after 3 h of irradiation. Pristine Vs-$ZnIn_2S_4$, with abundant sulfur vacancies, exhibited improved performance (2.45 μmol of H_2 under identical conditions), attributable to its Urbach band tail absorption that extends its photo-response into the NIR region beyond UV/visible light.[7,35,42] Upon coupling CuSe with Vs-$ZnIn_2S_4$, NIR-driven H_2 production was significantly enhanced. Specifically, 0.5 wt% CuSe loading yielded 6.42 μmol of H_2 after 3 h, while 1 wt% loading increased H_2 evolution to 11.6 μmol. However, a higher loading of 2 wt% reduced H_2 production to 3.3 μmol, indicating that optimal CuSe loading (around 1 wt%) results in the best balance between NIR light absorption and efficient electron transfer.[43,44] Comparative studies of sacrificial agents (Fig. S6) confirmed that TEOA provides the highest H_2 evolution, likely due to its effective electron donation and catalyst stabilization.[45] Consequently, TEOA was selected for subsequent photocatalytic tests. The Z@$Cu_{(1\ wt\%)}$ composite demonstrated sustained activity

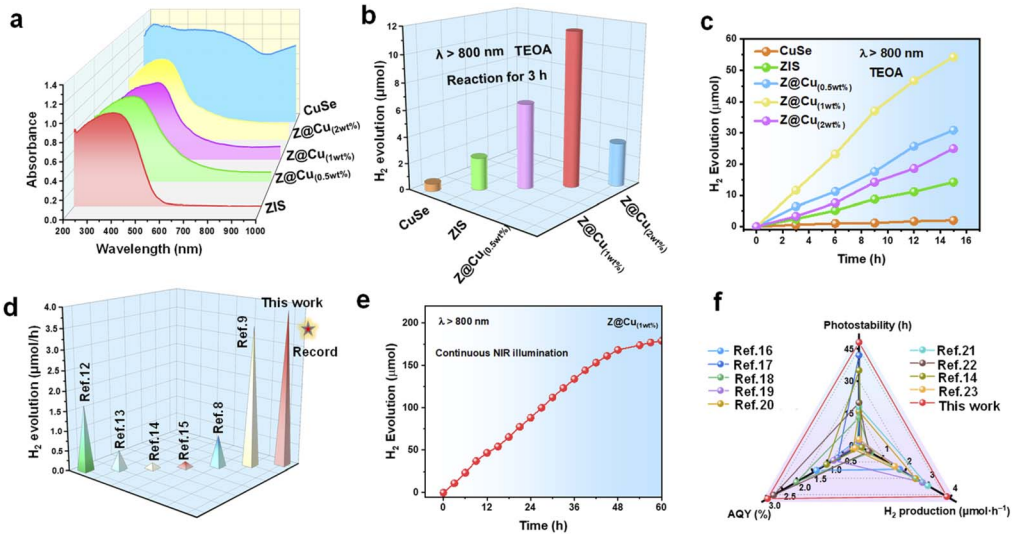

Fig. 2 (a) UV-vis-NIR absorption spectra of pristine CuSe and Vs-$ZnIn_2S_4$, and their composites. (b) H_2 production performance of pristine CuSe and Vs-$ZnIn_2S_4$, and their corresponding composites under NIR light (λ > 800 nm) for 3 hours. (c) H_2 production rates of pristine CuSe and Vs-$ZnIn_2S_4$, and their corresponding composites under NIR light (λ > 800 nm) over time. (d) Comparison of the H_2 production activity with previously reported plasmonic photocatalysts under NIR light. (e) Photostability evaluation under continuous NIR light irradiation (λ > 800 nm). (f) Photostability, H_2 production rate, and AQE under monochromatic NIR light, compared with currently reported NIR-responsive photocatalytic systems under similar conditions.

with 54.2 μmol of H_2 generated over 15 h (Fig. 2c), highlighting its potential for practical NIR-driven water splitting. Notably, this catalyst outperformed previously reported plasmonic photocatalytic systems in the half-reaction of water splitting (Fig. 2d & Table S1), underscoring its efficiency in NIR light utilization. Moreover, the optimal sample achieved a high H_2 evolution rate of 2.18 μmol h^{-1} at $\lambda = 940$ nm, corresponding to an apparent quantum efficiency (AQE) of 3.0%. To our knowledge, this represents the best performance reported for noble-metal-free hybrid photocatalysts at wavelengths above 900 nm (Table S2), providing a valuable benchmark for future NIR-responsive photocatalyst design. Additionally, the stability of photocatalysts is essential for their reliability, longevity, and economic feasibility in practical applications.[46] The $Z@Cu_{(1\ wt\%)}$ composite maintained stable performance over 48 h of continuous NIR irradiation (Fig. 2e). In a nine-cycle stability experiment, the photocatalytic activity showed almost no degradation compared to the initial run (Fig. S7). XRD patterns collected before and after cycling revealed no significant structural changes, confirming the material's robustness (Fig. S8). Remarkably, $Z@Cu_{(1\ wt\%)}$ also retained both structural integrity and catalytic function under strongly acidic (pH = 1) and strongly alkaline (pH = 12) conditions (Fig. S9 and S10), in striking contrast to the degradation or phase transformation commonly observed for many photocatalysts in such harsh environments. Moreover, the material exhibited excellent stability in high-salt media, indicating strong resistance to ionic interference (Fig. S11)—a crucial feature for practical applications involving saline or seawater sources. To the best of our knowledge, the overall stability of $Z@Cu_{(1\ wt\%)}$ surpasses that of all previously reported non-noble-metal NIR-driven photocatalytic systems (Fig. 2f and Table S3).

Charge separation and transfer ability

To elucidate the enhanced photocatalytic activity, a series of electrochemical and photophysical characterization studies were conducted. Beyond light absorption, efficient separation of photogenerated carriers critically governs photocatalytic performance.[47] Transient photocurrent measurements revealed that under NIR illumination, the current response increased with CuSe loading up to 1 wt% but declined at 2 wt% (Fig. S12), mirroring the photocatalytic activity trend. $Z@Cu_{(1\ wt\%)}$ exhibited a photocurrent density of ~3.24 μA cm^{-2}, markedly higher than that of pristine Vs-$ZnIn_2S_4$ (0.27 μA cm^{-2}), indicating enhanced charge separation upon CuSe integration.[48] Electron paramagnetic resonance (EPR) analysis using DMPO as a trapping agent further confirmed improved carrier separation. Under NIR light, $Z@Cu_{(1\ wt\%)}$ showed a substantially stronger $^{\cdot}O^{2-}$ signal than pure Vs-$ZnIn_2S_4$ (Fig. S13), consistent with more efficient photogenerated carrier separation.[49] Electrochemical impedance spectroscopy (EIS) Nyquist plots displayed a smaller semicircle for $Z@Cu_{(1\ wt\%)}$ compared to Vs-$ZnIn_2S_4$ (Fig. S14), suggesting facilitated interfacial charge transfer.[50] Additionally, photoluminescence (PL) spectra demonstrated significant quenching for $Z@Cu_{(1\ wt\%)}$ relative to the pristine counterpart (Fig. S15), corroborating suppressed charge recombination and enhanced separation efficiency.[51]

Mechanism study

To elucidate the NIR-driven water-splitting mechanism, the carrier dynamics in the Vs-$ZnIn_2S_4$@CuSe plasmonic composite were investigated using femtosecond transient absorption (fs-TA) spectroscopy. Upon 400 nm excitation and probing from 820 to 1400 nm (Fig. 3a and b), both ZIS and $Z@Cu_{(1\ wt\%)}$ show

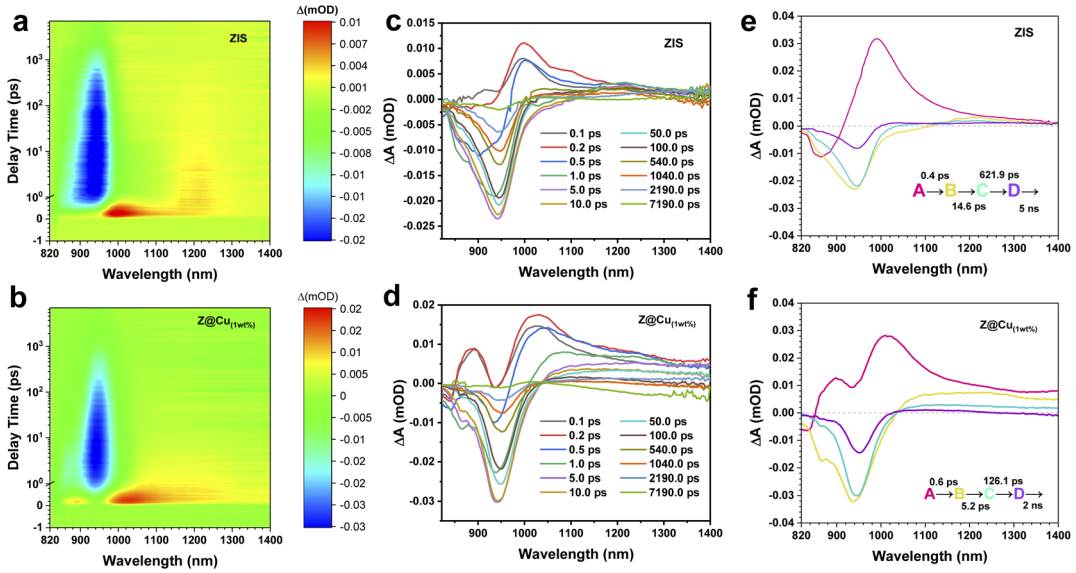

Fig. 3 (a and b) Two-dimensional (2D) pseudo-colour plot of NIR-region transient absorption spectra, with excitation at 400 nm, for pristine Vs-$ZnIn_2S_4$ and Z@Cu(1 wt%), respectively. [*X*-axis: probe wavelength; *Y*-axis: pump–probe delay; colors represent the change in absorbance (ΔA) in milli-optical density units (mOD)]. (c and d) Transient absorption (TA) spectra at different time delays, with excitation at 400 nm, for pristine Vs-$ZnIn_2S_4$ and $Z@Cu_{(1\ wt\%)}$, respectively. Global fitting analysis of the species-associated difference spectra (SADS) for (e) ZIS and (f) $Z@Cu_{(1\ wt\%)}$.

negative signals (stimulated emission, SE) at 890–980 nm, consistent with their steady-state fluorescence (Fig. S15). While ZIS exhibits two excited-state absorption (ESA) bands (960–1160 nm and 1160–1400 nm) with distinct kinetics, $Z@Cu_{(1\ wt\%)}$ presents an additional ESA band at 840–940 nm, attributed to CuSe modification. Temporal evolution analysis (Fig. 3c and d) reveals positive ESA signals in both samples following excitation (ZIS: 960–1400 nm; $Z@Cu_{(1\ wt\%)}$: 840–940 nm + 960–1400 nm). Within the initial sub-picosecond regime (0–1 ps), these ESA features decay rapidly, accompanied by the emergence of negative SE bands at 890–980 nm. For ZIS, ESA at 960–1160 nm vanishes, leaving only the 1160–1400 nm band. For $Z@Cu_{(1\ wt\%)}$, ESA at 840–940 nm and 960–1060 nm vanishes, leaving only the 1060–1400 nm band. Subsequently (1–10 ps), the SE bands in both samples narrow progressively and undergo red-shifting, while long-wavelength ESA components gradually diminish. At longer time scales (10–100 ps), the SE bands in both samples further weaken with slight additional red-shifting, concurrent with continued decay of the residual ESA signals. Finally, within the instrument response window (up to 7 ns), all transient signals nearly fully decay. Notably, $Z@Cu_{(1\ wt\%)}$ exhibits significantly shorter excited-state lifetimes than ZIS, revealing accelerated relaxation dynamics induced by CuSe modification. Global fitting analysis of the transient absorption data (Fig. 3e and f) reveals distinct species-associated difference spectra (SADS). For ZIS, the initial species (Species A, red trace) exhibits an SE band at 820–920 nm and a pronounced excited-state absorption (ESA) feature centered near 1000 nm. This excited-state species forms instantaneously upon photoexcitation. Subsequently, an ultrafast sub-500 fs relaxation (0.4 ps) populates Species B (yellow trace), characterized by: (i) the disappearance of the ~1000 nm ESA, (ii) the emergence of a new SE band at ~940 nm, and (iii) the appearance of an additional ESA band spanning 1100–1400 nm. This distinct spectral evolution unequivocally establishes Species A and B as separate excited-state entities, with the transformation directly attributable to the incipient stage of charge separation.[52] Subsequently, Species B transforms into Species C (cyan) at 14.6 ps, accompanied by a narrowing of the SE signal. The B → C process may be attributed to the recombination of electrons and holes in the bulk phase.[53] Meanwhile, the excited-state absorption (ESA) signal at longer wavelengths gradually weakens. This is followed by the conversion of Species C to Species D (purple) on a longer timescale (621.9 ps), during which the SE signal and the long-wavelength ESA signal progressively diminish. Concurrently, a new ESA signal emerges around 1000 nm, indicating relaxation to a new excited state. The C → D process is attributed to a charge transfer route.[54] Finally, Species D almost completely decays within the experimental time window, with a fitted lifetime of 5 ns, which is tentatively attributed to a charge recombination process.[32] Upon CuSe composite formation, the $Z@Cu_{(1\ wt\%)}$ sample exhibits an additional excited-state absorption (ESA) signal around 900 nm in the initial excited state species A (red) compared to pristine ZIS, which is attributed to the modification with CuSe. The subsequent excited-state transformation features spectral similarities to those of ZIS. Specifically, the A → B process generates a new SE signal and an ESA signal beyond 1050 nm. The timescale of this process is comparable to that observed in ZIS, indicating that the introduction of CuSe does not affect this specific relaxation pathway. Subsequently, the B → C → D process, although spectrally identical to that in ZIS, exhibits a significantly

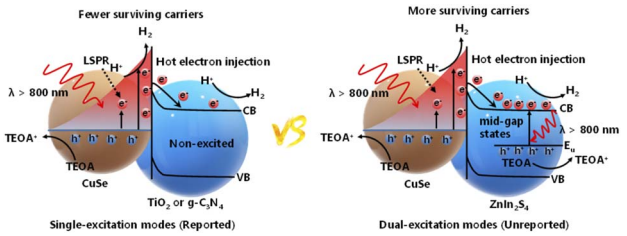

Fig. 4 Schematic of the newly developed plasmon-mediated photocatalysts using the earth-abundant copper chalcogenide (CuSe) for NIR-driven photocatalytic H_2 production. A possible band diagram and NIR-induced carrier dynamics in the plasmonic heterojunction are shown, illustrating the NIR light-driven photocatalytic reaction (E_u: the energy of the band tail, also referred to as the Urbach energy).

accelerated relaxation rate, and the C → D process (126.1 ps) is about five times faster. These results indicate that after CuSe modification, photogenerated carriers have more opportunities to migrate to the catalyst surface, thereby leading to enhanced water splitting performance. Additionally, kinetic traces at four wavelengths (860, 940, 1000, and 1200 nm) were selected for display (Fig. S16), demonstrating the high quality of the global fitting analysis. Furthermore, the temporal evolution profiles of species concentrations reveal that the relaxation times of the last three species (A, B, and C) in $Z@Cu_{(1\ wt\%)}$ are significantly faster than those in ZIS (Fig. S17).

Furthermore, the study compared two modes for the photocatalytic process: PMDE and PMSE (plasmon-mediated single-excitation) modes (Fig. S18). In the PMSE mode, the performance was mediocre when 1 wt% CuSe was combined with UV-responsive (TiO_2) or visible light-responsive ($g\text{-}C_3N_4$) semiconductors, suggesting that these combinations are less efficient in utilizing NIR photons for water splitting. However, in the PMDE mode, when 1 wt% CuSe was combined with NIR light-harvesting catalysts like Vs-$ZnIn_2S_4$, the performance improved remarkably. This suggests that PMDE is a more favorable approach for enhancing the NIR-driven photocatalytic process. The PMDE route seems to offer superior performance for NIR-driven water splitting because it likely promotes better electron excitation and charge separation when combined with NIR-responsive catalysts like Vs-$ZnIn_2S_4$. Building upon previously reported studies of NIR-responsive plasmonic photocatalysts and our experimental results, we propose a possible PMDE mechanism for NIR-driven water splitting (Fig. 4). Unlike traditional PMSE mechanisms for NIR-driven photoredox reactions, the PMDE pathway facilitates the generation of more surviving carriers that are essential for triggering efficient photocatalytic H_2 production. In this proposed possible mechanism, the plasmonic CuSe is photochemically excited *via* the LSPR effect under NIR light, generating hot electrons and holes. These plasmon-induced hot electrons can then be transferred from CuSe to the NIR-activated semiconducting phase (Vs-$ZnIn_2S_4$). This transfer allows for the accumulation of hot carriers, which are crucial for highly efficient NIR-driven H_2 production.

Theoretical calculation analysis

To further elucidate the electronic and catalytic properties of the Vs-$ZnIn_2S_4$@CuSe heterostructure, we performed density functional theory (DFT) calculations in this study. The spin-polarized DFT calculations were performed in the Device Studio-integrated Projector Augmented-Wave method package (DS-PAW), with the aid of DS-PAW for calculating the projected density of states (PDOS), Bader charge transfer, and charge density difference.[55] The optimized geometries of the Vs-$ZnIn_2S_4$@CuSe heterostructure are depicted in Fig. 5a and b. From these results, it can be inferred that the lattice mismatch ratio between Vs-$ZnIn_2S_4$ and CuSe is less than 3%, which is highly favorable for the formation of a well-integrated heterojunction. Additionally, the binding energy of the Vs-$ZnIn_2S_4$@CuSe heterostructure is found to be −5.03 eV per unit cell, indicating a strong interaction between the components, which is a crucial factor for ensuring the stability of NIR-driven water splitting within the heterostructure. The charge density difference diagram, shown in Fig. 5c, represents the regions of charge accumulation and depletion, providing insights into the electron redistribution at the interface of the heterostructure. A notable depletion of charge occurs in the CuSe component, while charge accumulation is observed in the Vs-$ZnIn_2S_4$ layer. Bader charge transfer analysis reveals an approximate charge transfer of 0.16 $|e|$ from CuSe to Vs-$ZnIn_2S_4$. This suggests that the electronic states are predominantly localized on the Vs-$ZnIn_2S_4$ side of the interface, further confirming the favorable electronic properties of this layer.[56] The projected density of states (PDOS) analysis offers additional insight into the contributions of both Vs-$ZnIn_2S_4$ and CuSe to the overall electronic properties of the heterostructure. As shown in Fig. 5d, the interaction between Cu 3d orbitals and Se 3p orbitals, along with the associated electron transitions, plays a pivotal role in the NIR light absorption capabilities of CuSe. The PDOS of CuSe reflects its metallic characteristics, with a significant number of electronic states at the Fermi level (E_f), especially those derived from the Cu 3d and Se 3p orbitals, which are indicative of its electrical conductivity. Fig. 5e demonstrates how the distinct orbital densities of states of S, In, and Zn in the Vs-$ZnIn_2S_4$ layer influence its NIR absorption properties. The presence of sulfur-rich defects enhances the optical absorption of the material, particularly in the NIR region, by generating localized states near the S 2p orbitals. The contributions from S 2p and In 4d orbitals are particularly crucial, as they facilitate NIR light absorption *via* orbital interactions and electronic transitions. Moreover, as shown in Fig. 5f, the incorporation of CuSe into Vs-$ZnIn_2S_4$ significantly improves the electronic conductivity of the composite, primarily due to orbital hybridization and electronic interactions at the heterojunction interface. One of the critical steps in NIR-driven water splitting is the efficient adsorption of protons and water molecules on the surface of the photocatalyst (Fig. 5g and h). Upon combining with CuSe, the ΔG_H value for the composite system drops drastically from 0.88 eV for pure Vs-$ZnIn_2S_4$ to 0.16 eV (Fig. 5i), suggesting that H_2 generation becomes significantly easier in the composite system compared to the pure counterpart. Furthermore, the adsorption energy of

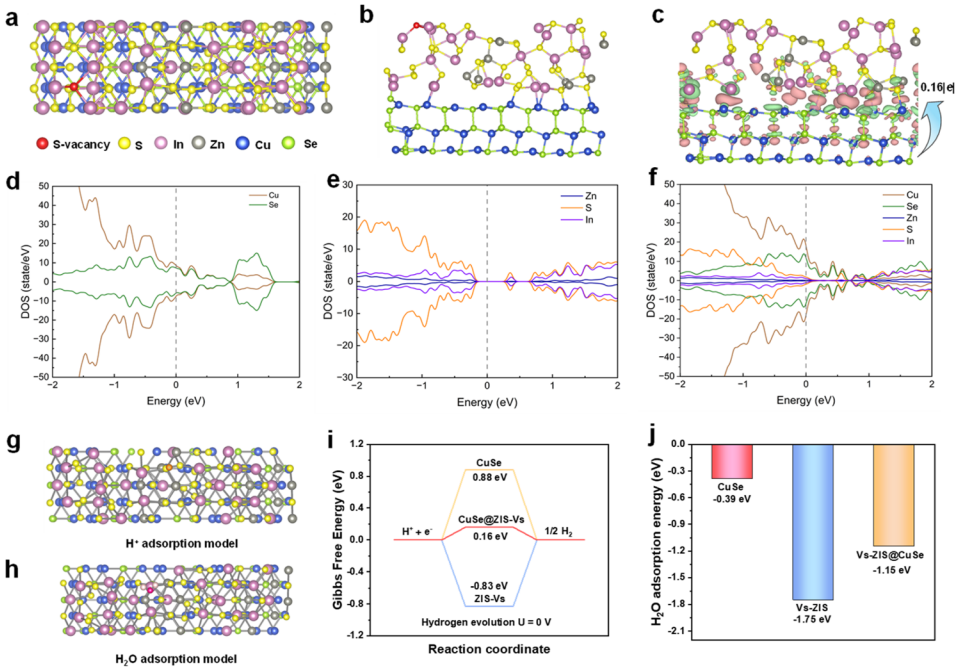

Fig. 5 (a) Top and (b) side views of the Vs-$ZnIn_2S_4$@CuSe heterostructural model. (c) Charge density difference diagram for the Vs-$ZnIn_2S_4$@CuSe heterostructure, where pink and green areas represent charge accumulation and charge depletion, respectively. The projected density of states (PDOS) of (d) CuSe, (e) Vs-$ZnIn_2S_4$, and (f) the Vs-$ZnIn_2S_4$@CuSe heterojunctions are shown, with the Fermi energy (E_f) set to zero at the midgap. (g) H^+ adsorption model for the Vs-$ZnIn_2S_4$@CuSe heterojunction. (h) H_2O adsorption model for the Vs-$ZnIn_2S_4$@CuSe heterojunction. (i) Gibbs free energy curves for the hydrogen evolution reaction (HER) process on CuSe, Vs-$ZnIn_2S_4$, and Vs-$ZnIn_2S_4$@CuSe heterojunctions, respectively. (j) H_2O adsorption energy for CuSe, Vs-$ZnIn_2S_4$, and Vs-$ZnIn_2S_4$@CuSe heterojunctions, respectively.

water molecules is notably negative for Vs-$ZnIn_2S_4$@CuSe, indicating that water molecules are readily adsorbed onto the surface (Fig. 5j). This enhanced adsorption property is highly beneficial for NIR-driven photocatalytic water splitting, as it facilitates efficient interaction between the photocatalyst and water molecules.

Conclusions

In summary, we report on the controlled regulation of a plasmonic nanocomposite photocatalyst (Vs-$ZnIn_2S_4$@CuSe), which enables the demonstration of unique PMDE modes for highly efficient and stable NIR-driven H_2 production. Photoelectrochemical characterization combined with theoretical calculations confirmed that the unique LSPR effect of CuSe species enhances NIR photon absorption, facilitates hot carrier generation, reduces the reaction energy barrier, inhibits charge recombination, and triggers interfacial charge redistribution synergistically. The optimized Vs-$ZnIn_2S_4$@CuSe nanohybrid achieves a superior H_2 production rate of 2.18 μmol h^{-1} with an apparent quantum efficiency (AQE) of 3.0% at $\lambda = 940$ nm, representing the highest value reported to date for noble-metal-free hybrid photocatalysts at wavelengths exceeding 900 nm. Moreover, the optimized catalyst maintains long-term structural stability under harsh conditions including strong acidic, basic and high-salinity environments during continuous NIR light irradiation. This rational heterostructural interfacial coupling strategy presents an innovative paradigm for designing and constructing highly efficient and ultrastable NIR-responsive photocatalysts *via* PMDE. This PMDE-derived interfacial coupling strategy can be further extended to other plasmonic–semiconductor systems to harvest low-energy photons for diverse catalytic applications in the future.

Author contributions

Conceptualization: Yuanyong Huang and Weidong Shi. Formal analysis: Yuanyong Huang, Cai Ning, Yu Yu, Zhongkai Xie, and Hailing Huo. Funding acquisition: Yuanyong Huang, Cai Ning, Yu Yu, Zhongkai Xie, Hailing Huo, and Weidong Shi. Investigation: Yuanyong Huang, Xinyu Lu, Yang Chao, Junhao He, and Qiankun Gao. Methodology: Yuanyong Huang, Xinyu Lu, Yang Chao, Junhao He, and Qiankun Gao. Supervision: Weidong Shi. Writing – original draft: Yuanyong Huang and Weidong Shi. Writing – review & editing: Yuanyong Huang, Cai Ning, and Weidong Shi. All authors contributed to the discussion of the results and the preparation of the manuscript.

Conflicts of interest

There are no conflicts to declare.

Data availability

The authors declare that the data supporting the findings of this study are available within the article and its supplementary

information (SI). Supplementary information is available. See DOI: https://doi.org/10.1039/d6sc01125j.

Acknowledgements

This work was supported by the National Natural Science Foundation of China (22225808, U24A20551, 22508148, 22503039, 2240082215), Jiangsu Province Innovation Support Program International Science and Technology Cooperation Project (BZ2022045), Natural Science Foundation of Jiangsu Province (BK20251008, BK20251012), Science and Technology Bureau of Zhenjiang (JC2025024), High-level Talent Cultivation Project of Jiangsu University of Science and Technology (1112932503, 1112932403, 1112932402, 1112932603) and the Special Scientific Research Project of School of Emergency Management, Jiangsu University (KY-A-02). Author Weidong Shi was partially supported by the postgraduate research opportunities program of HZWTECH (HZWTECH-PROP).

Notes and references

1 P. Zhou, I. A. Navid, Y. J. Ma, Y. X. Xiao, P. Wang, Z. W. Ye, B. W. Zhou, K. Sun and Z. T. Mi, *Nature*, 2023, **613**, 66–70.
2 B. Su, K. Tang, J. J. Cai, X. H. Lin, W. D. Xing, K. L. Liu, X. F. Lu, Y. D. Hou, W.-J. Ong and S. B. Wang, *ACS Catal.*, 2026, **16**(5), 5208–5217.
3 M. Hartkorn, R. Kampes, F. Müller, L. Zedler, A. Edwards, P. Rohland, A. K. Mengele, S. Zechel, M. D. Hager, B. Dietzek-Ivanšić, M. Schmitt, J. Popp, U. S. Schubert and S. Rau, *Nat. Commun.*, 2026, **17**, 1141.
4 R. T. Chen, Z. F. Ren, Y. Liang, G. H. Zhang, T. Dittrich, R. Z. Liu, Y. Liu, Y. Zhao, S. Pang, H. Y. An, C. W. Ni, P. W. Zhou, K. L. Han, F. T. Fan and C. Li, *Nature*, 2022, **610**, 296–301.
5 A. Rodríguez-Camargo, M. W. Terban, M. Paetsch, E. A. Rico, D. Graf, R. Hirpara, V. Duppel, I. Moudrakovski, M. Etter, N. Guijarro, C. Ochsenfeld, R. E. Dinnebier, L. Yao and B. V. Lotsch, *Nat. Synth.*, 2025, **4**, 710–719.
6 Y. Y. Huang, D. Li, S. Feng, Y. J. Jia, S. H. Guo, X. J. Wu, M. Chen and W. D. Shi, *Angew. Chem., Int. Ed.*, 2022, **61**(45), e202212234.
7 Y. Y. Huang, H. Yang, S. Feng, C. W. Ma, P. Y. Cao, F. F. Li, X. Y. Lu and W. D. Shi, *Sci. China Mater.*, 2024, **67**, 1812–1819.
8 N. Li, H. K. Fan, Y. J. Dai, J. Kong and L. Ge, *Appl. Surf. Sci.*, 2020, **508**, 145200.
9 W. H. Xue, H. L. Sun, X. Y. Hu, X. Bai, J. Fan and E. Z. Liu, *Chin. J. Catal.*, 2022, **43**(2), 234–245.
10 P. Y. Hsieh, J. Y. Wu, T. F. M. Chang, C. Y. Chen, M. Sone and Y. J. Hsu, *Arab. J. Chem.*, 2020, **13**, 8372–8387.
11 L. L. Wang, R. J. Sa, Y. C. Wei, X. F. Ma, C. G. Lu, H. W. Huang, E. Fron, M. Liu, W. Wang, S. P. Huang, J. Hofkens, M. B. J. Roeffaers, Y.-J. Wang, J. H. Wang, J. L. Long, X. Z. Fu and R. S. Yuan, *Angew. Chem., Int. Ed.*, 2022, **61**(39), e202204561.
12 R. Yu, B. F. Luo, M. Chen, D. B. Xu, X. J. Wu, D. Li, Y. Y. Huang, Z. K. Xie, N. J. Shen, S. C. Meng and W. D. Shi, *Int. J. Hydrogen Energy*, 2023, **48**(63), 24285–24294.
13 Z. C. Lian, Y. Kobayashi, J. J. M. Vequizo, C. S. K. Ranasinghe, A. Yamakata, T. Nagai, K. Kimoto, K. Kobayashi, K. Tanaka, T. Teranishi and M. Sakamoto, *Nat. Sustain.*, 2022, **5**, 1092–1099.
14 Z. C. Lian, F. Wu, J. Z. Zi, G. S. Li, W. Wang and H. X. Li, *J. Am. Chem. Soc.*, 2023, **145**(28), 15482–15487.
15 Z. C. Lian, M. Sakamoto, J. J. M. Vequizo, C. S. K. Ranasinghe, A. Y. Takuro, N. K. Yoichi, K. N. Tamai and T. Teranishi, *J. Am. Chem. Soc.*, 2019, **141**(6), 2446–2450.
16 X. Y. Cai, M. S. Zhu, O. A. Elbanna, M. Fujitsuka, S. Kim, L. Mao, J. Y. Zhang and T. Majima, *ACS Catal.*, 2018, **8**(1), 122–131.
17 Z. C. Lian, F. Wu, Y. Q. Zhong, J. Z. Zi, Z. Li, X. Wang, T. Nakagawa, H. X. Li and M. Sakamoto, *Appl. Catal., B*, 2022, **318**, 121860.
18 M. S. Zhu, C. Y. Zhai, M. Fujitsuka and T. Majima, *Appl. Catal., B*, 2018, **221**, 645–651.
19 Y. S. Xu, M. J. Fan, W. J. Yang, Y. H. Xiao, L. T. Zeng, X. Wu, Q. H. Xu, C. L. Su and Q. J. He, *Adv. Mater.*, 2021, **33**(39), 2101455.
20 G. Q. Zhang, Y. S. Xu, M. Rauf, J. Y. Zhu, Y. L. Li, C. X. He, X. Z. Ren, P. X. Zhang and H. W. Mi, *Adv. Sci.*, 2022, **9**(21), 2201677.
21 S. S. Huang, Y. X. Zhang, C. F. Du and Y. G. Su, *Chem. Commun.*, 2020, **56**(45), 6054–6057.
22 Y. Y. Huang, Y. P. Jian, L. H. Li, D. Li, Z. Y. Fang, W. X. Dong, Y. H. Lu, B. F. Luo, R. J. Chen, Y. C. Yang, M. Chen and W. D. Shi, *Angew. Chem., Int. Ed.*, 2021, **60**(10), 5245–5249.
23 Y. Lu, X. F. Jia, Z. Y. Ma, Y. Li, S. Yue, X. F. Liu and J. Y. Zhang, *Adv. Funct. Mater.*, 2022, **32**(35), 2203638.
24 C. W. Tsao, S. Narra, J. C. Kao, Y.-C. Lin, C.-Y. Chen, Y.-C. Chin, Z.-J. Huang, W.-H. Huang, C.-C. Huang, C.-W. Luo, J.-P. Chou, S. Ogata, M. Sone, M. H. Huang, T.-F. M. Chang, Y.-C. Lo, Y.-G. Lin, E. W.-G. Diau and Y.-J. Hsu, *Nat. Commun.*, 2024, **15**, 413.
25 L. Ma, D. J. Yang, X. P. Song, H.-X. Li, S.-J. Ding, L. Xiong, P.-L. Qin and X.-B. Chen, *Sol. RRL*, 2020, **4**(1), 1900376.
26 J. Y. Qin and H. P. Zeng, *Appl. Catal., B*, 2017, **209**, 161–173.
27 Z. L. Xia, R. Yu, H. Yang, B. F. Luo, Y. Y. Huang, D. Li, J. Y. Shi and D. B. Xu, *Int. J. Hydrogen Energy*, 2022, **47**(27), 13340–13350.
28 M. S. Zhu, S. Kim, L. Mao, M. Fujitsuka, J. Y. Zhang, X. C. Wang and T. Majima, *J. Am. Chem. Soc.*, 2017, **139**(37), 13234–13242.
29 B. Lin, R. H. Duan, Y. H. Li, W. B. Hua, Y. Zhou, J. D. Zhou, J. Di, X. Luo, H. Li, W. T. Zhao, G. D. Yang, Z. Liu and F. C. Liu, *Adv. Mater.*, 2024, **36**(32), 2404833.
30 N. Li, Y. P. Qiu, L. P. Li, J. T. Zhang, S. F. Xu, Y. Q. Gao and L. Ge, *Sep. Purif. Tecnol.*, 2025, **353**, 128305.
31 N. Li, H. K. Fan, W. W. Zhao, Y. Q. Gao and L. Ge, *Appl. Surf. Sci.*, 2022, **590**, 153028.

32 H. B. Chen, Y. J. Xing, S. T. Liu, J. L. Fu, H. L. Shi, Y. J. Liang, L. J. Wang and W. Z. Wang, *J. Colloid Interface Sci.*, 2022, **613**, 103–116.
33 Y. C. Wang, M. J. Liu, C. X. Wu, J. P. Gao, M. Li, Z. P. Xing, Z. Z. Li and W. Zhou, *Small*, 2022, **18**(31), 2270167.
34 M. Huang, X. Wang, G. X. Jing, C. C. Meng, Y. C. Li, X. H. Li, L. Z. Fan, Y. Wan and S. H. Yang, *J. Phys. Chem. Lett.*, 2021, **12**(33), 7988–7996.
35 H. Yang, Y. Y. Huang, B. F. Luo, Z. K. Xie, D. Li, D. B. Xu, Y. Lei and W. D. Shi, *Chem. Commun.*, 2024, **60**, 1035–1038.
36 Y. H. Li, M. Y. Qi, Z. R. Tang and Y. J. Xu, *J. Phys. Chem. C*, 2022, **126**(4), 1872–1880.
37 X. W. Ruan, S. L. Zhao, M. H. Xu, D. X. Jiao, J. Leng, G. Z. Fang, D. P. Meng, Z. F. Jiang, S. Y. Jin, X. Q. Cui and S. K. Ravi, *Adv. Energy Mater.*, 2024, **14**(36), 2401744.
38 S. N. Li, L. X. Meng, W. Tian and L. Li, *Adv. Energy Mater.*, 2022, **12**(22), 2200629.
39 Z. Z. Chen, Y. J. Yan, K. Q. Sun, L. Tan, F. Guo, X. Du and W. L. Shi, *J. Colloid Interface Sci.*, 2024, **661**, 12–22.
40 N. Li, L. P. Li, Y. P. Qiu, X. H. Liu, J. T. Zhang, Y. Q. Gao and L. Ge, *Nanocale*, 2024, **16**, 8151–8161.
41 X. L. Liu, B. B. Huang, J. Li, B. J. Li and Z. Z. Lou, *Mater. Horiz.*, 2024, **11**, 5470–5498.
42 X. J. Wu, D. Li, B. F. Luo, B. Y. Chen, Y. Y. Huang, T. T. Yu, N. J. Shen, L. H. Li and W. D. Shi, *Appl. Catal., B*, 2023, **325**, 122292.
43 J. T. Lee, H. H. Tseng and M. Y. Wey, *Sol. Energy*, 2022, **231**, 949–957.
44 W. H. Lee, C. W. Lee, G. D. Cha, B.-H. Lee, J. H. Jeong, H. Park, J. Heo, M. S. Bootharaju, S.-H. Sunwoo, J. H. Kim, K. H. Ahn, D.-H. Kim and T. Hyeon, *Nat. Nanotechnol.*, 2023, **18**, 754–762.
45 A. Sherryna, M. Tahir and Z. Y. Zakaria, *Int. J. Hydrogen Energy*, 2024, **51**, 1511–1531.
46 Y. F. Chen, L. Soler, C. Cazorla, J. Oliveras, N. G. Bastús, V. F. Puntes and J. Llorca, *Nat. Commun.*, 2023, **14**, 6165.
47 Z. A. Khalil, A. Nath, K. Hannouche, N. Assaad, G. Mouchaham, A. Beauvois, V. Briois, C. Serre, M. Hmadeh, M. Daturi and M. El-Roz, *Nat. Commun.*, 2026, **17**, 308.
48 D. Tan, T. F. Ding, K. d. Shen, C. Xu, S. Jin, D. Q. Hu, S. Sun and M. Z. Zhu, *Chem. Sci.*, 2025, **16**, 9326–9336.
49 X. F. Zhou, J. M. Li, X. Cai, Q. Z. Gao, S. S. Zhang, S. Y. Yang, H. Q. Wang, X. H. Zhong and Y. P. Fang, *J. Mater. Chem. A*, 2020, **8**, 17120–17127.
50 Q. S. Nan, J. Ning, B. Han, H. T. Wei, X. F. Wang, Y.-Y. Gu, S. X. Zhou, G. Q. Cao, G. Z. Zhang, X. H. Li, Y. G. Jia and L. Hao, *Chem. Sci.*, 2026, **17**, 466–474.
51 S. K. Xue, H. Tang, M. Shen, X. C. Liang, X. Y. Li, W. D. Xing, C. Yang and Z. Y. Yu, *Adv. Mater.*, 2024, **36**(16), 2311937.
52 D. Sebastian, A. Pallikkara, H. Bhatt, H. N. Ghosh and K. Ramakrishnan, *J. Phys. Chem. C*, 2022, **126**(27), 11182–11192.
53 F. Chen, T. Y. Ma, T. R. Zhang, Y. H. Zhang and H. W. Huang, *Adv. Mater.*, 2021, **33**(10), 2005256.
54 C. Cheng, J. Zhang, B. Zhu, G. Liang, L. Zhang and J. Yu, *Angew. Chem., Int. Ed.*, 2023, **62**(8), e202218688.
55 P. E. Blöchl, *Phys. Rev. B: Condens. Matter Mater. Phys.*, 1994, **50**(24), 17953.
56 C. Ning, Y. Yu, Z. H. Yang, Y. H. Wang and W. D. Shi, *Chem. Phys. Lett.*, 2024, **856**, 141637.